China Ocean Eng., Vol. 29, No. 2, pp. 223 – 240

DOI 10.1007/s13344-015-0016-0, ISSN 0890-5487

A Geometrically Exact Formulation for Three-Dimensional Numerical Simulation of the Umbilical Cable in A Deep-Sea ROV System*

QUAN Wei-cai (全伟才)[a, b, 1], ZHANG Zhu-ying (张竺英)[a], ZHANG Ai-qun (张艾群)[a], ZHANG Qi-feng (张奇峰)[a] and TIAN Yu (田　宇)[a]

[a] *State Key Laboratory of Robotics*, *Shenyang Institute of Automation*, *Chinese Academy of Sciences*, *Shenyang 110016*, *China*

[b] *University of Chinese Academy of Sciences*, *Beijing 100049*, *China*

(Received 2 December 2013; received revised form 10 March 2014; accepted 10 April 2014)

ABSTRACT

This paper proposes a geometrically exact formulation for three-dimensional static and dynamic analyses of the umbilical cable in a deep-sea remotely operated vehicle (ROV) system. The presented formulation takes account of the geometric nonlinearities of large displacement, effects of axial load and bending stiffness for modeling of slack cables. The resulting nonlinear second-order governing equations are discretized spatially by the finite element method and solved temporally by the generalized-α implicit time integration algorithm, which is adapted to the case of varying coefficient matrices. The ability to consider three-dimensional union action of ocean current and ship heave motion upon the umbilical cable is the key feature of this analysis. The presented formulation is firstly validated, and then three numerical examples for the umbilical cable in a deep-sea ROV system are demonstrated and discussed, including the steady configurations only under the action of depth-dependent ocean current, the dynamic responses in the case of the only ship heave motion, and in the case of the combined action of the ship heave motion and ocean current.

Key words: *umbilical cable*; *cable dynamics*; *deep-sea ROV*; *dynamic modeling*

1. Introduction

For underwater operation tasks, such as installations, maintenances and impairments, deep-sea remotely operated vehicles (ROVs) have been applied widely (Yan *et al*., 2005; Feng *et al*., 2011), which are typically composed of a supporting ship, an umbilical cable, a tether-management-system (TMS, also named cage) and a ROV (Driscoll *et al*., 2000a), as shown in Fig. 1. The umbilical cable plays a significant role in deep sea ROV systems, such as the physical link, real-time transmission of information and lifeline, which make the ROV work effectively. The internal parts of an umbilical cable are composed of fiber-optic micro cables, and the outer parts are armored by steel wire or enveloped by high-strength synthetic fiber materials. One terminal of the umbilical cable holds the cage, which acts as the ballast, and can reduce the environmental disturbances on the ROV. However, through the umbilical cable the motion of supporting ship can be passed to the cage, which keeps

* This research was financially supported by the National High Technology Research and Development Program of China (863 Program, Grant No. 2008AA09Z201).

1 Corresponding author. Email: quanweicai@163.com

moving up and down, leading to large tension fluctuation in the umbilical cable. Moreover, the safety of submarine operation of the whole underwater system is affected, and the launch and recovery of ROV will be more difficult. To understand the complex dynamic characteristics of the entire underwater cable system under ocean currents or ship motions, modeling and analysis of the nonlinear dynamics of an underwater umbilical cable are needed, especially of its geometric nonlinearities due to the large displacement of the cable.

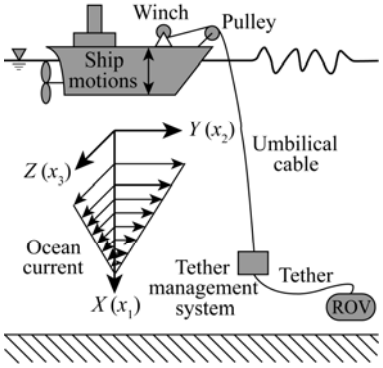

Fig. 1. A schematic of a typical deep-sea ROV system.

There are plenty of works on dynamics modeling of marine cables, and the numerical analysis of these flexible structures can be classified into three main methods: the finite difference method, the lumped mass method, and the finite element method. Ablow and Schechter (1983) proposed a numerical model for underwater towed cable using the finite difference method. Driscoll *et al*. (2000a) presented an one-dimensional finite element model consisting of linear viscoelastic element, which could accurately predict the heave motion of a cage under several different sea states. Wu and Chwang (2001) proposed a hydrodynamic model of a two-part underwater maneuverable towed system using the finite difference method, which provided an effective approach to determine the hydrodynamic characteristics of an underwater vehicle. However, the works above did not consider the effect of bending stiffness. When the cable tension is zero, a singular point will appear in the cable equation, which will cause interruption of the equation's calculation. In order to allow the cable equation to be suitable for low tension problem, Buckham *et al*. (2003a, 2003b) considered the effects of the bending and torsional stiffness of the cable, and established a low tension cable model using the lumped mass method, which proved that it can capture the dynamics at the low tension state by the tank experiment. Park *et al*. (2003) also considered the bending stiffness of towed cable, and presented a numerical investigation for a towed array sonar system by employing the finite difference method. Gobat and Grosenbaugh (2006) developed a computer program named WHOI Cable, whose governing equations include the effects of geometric and material nonlinearities, and bending stiffness. The program uses the finite difference method to discretize the ocean cable structures and analyzes the static and dynamic responses of time domain in vertical plane. Fang *et al*. (2013) presented a finite element model with cubic spline interpolation function to predict the deformation of a cable in the towed system.

In addition to the effects of axial load and bending, the deformation of an actual cable should also include the effects of shear and torsion and the actual cable moves in a three-dimensional space. However, the above works do not take into account these deformation factors completely, and most of

them are restrained in the two-dimensional plane. These problems can be avoided by using the geometrically exact beam theory which uses the position coordinate of centerline and the finite rotation of cross-section to describe the cable configuration. Reissner (1972) firstly proposed a two-dimensional geometrical exact beam model for static problem. After that, Simo and Vu-Quoc (1986) extended the two-dimensional geometrical exact beam theory to three dimension for static and dynamic problems. Cardona and Geradin (1988) illustrated that the finite element formulation of the geometrical exact beam could be divided into three classes, including the total Lagrangian formulation, the updated Lagrangian formulation, and the Euler formulation.

This paper extends the total Lagrangian formulation of the geometrically exact beam theory to the dynamic modeling of a three-dimensional umbilical cable, and investigates some important characteristics of the cable under various influences such as supporting ship heave motion, ocean currents, and different cable length of working depth. The characteristics mainly include the static and dynamic configurations of the cable, the tension of both ends of the cable, and the motion of the cage. This paper is organized as follows. In Section 2 we present the geometrically exact formulation applied to underwater umbilical cables. Section 3 describes the finite element discretization of the governing equations. In order to solve the second order nonlinear differential equations, in Section 4 we adopt the generalized-α method to the case of varying coefficient matrices. In Section 5, we give some numerical cases, including the steady cable configurations in a steady ocean current that is depth-dependent, the dynamic responses of the umbilical cable system with ship heave motion, and the dynamic responses of the umbilical cable system with both ship heave motion and ocean current.

2. Mathematical Formulation

2.1 Cable Kinematics

In this paper, we assume that the material of the umbilical cable is continuous, the initial state is straight, and the cross section is circular and symmetrical. As shown in Fig. 2, three coordinate frames are defined.

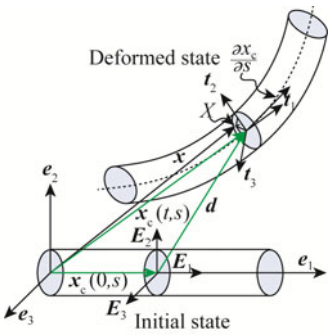

Fig. 2. Cable kinematics in a three-dimensional space.

The frame $\{\boldsymbol{e}_i\}$ is the inertial reference system fixed in the three-dimensional space with its corresponding coordinates $\{x_1, x_2, x_3\}$. The frame $\{\boldsymbol{E}_i\}$ is called the material coordinate system with its coordinates $\{X_1, X_2, X_3\}$; E_1 is tangent to the initial center line; $\boldsymbol{E}_2$ and $\boldsymbol{E}_3$ are located at

the cross-section of the beam initially, and for simplicity, it is assumed that $\boldsymbol{e}_i \equiv \boldsymbol{E}_i$ $(i=1,\ 2,\ 3)$. The frame $\{\boldsymbol{t}_i\}$ is a floating system, which coincides with the material frame $\{\boldsymbol{E}_i\}$ initially. During the process of deformation, the cross section initially perpendicular to the beam centerline is always a plane, and does not wrap. Owing to the shear effect, the tangent line of the beam center line $\partial \boldsymbol{x}_c / \partial s$ is not necessarily perpendicular to the beam cross section at the initial arc length s. The basis vectors of these three frames are related by

$$\boldsymbol{E}_i(s) = \boldsymbol{\Lambda}_0(s)\boldsymbol{e}_i,\ \boldsymbol{t}_i(t,s) = \boldsymbol{\Lambda}(t,s)\boldsymbol{E}_i(s), \tag{1}$$

where t is time and s is the initial arc length along the cable. $\boldsymbol{\Lambda}_0$ and $\boldsymbol{\Lambda}$ are the orthogonal tensor operators, satisfying the relationship $\boldsymbol{\Lambda}\boldsymbol{\Lambda}^{\mathrm{T}} = \boldsymbol{I}$. The current rotation operator $\boldsymbol{\Lambda}$ can be parameterized by the total rotation vector $\boldsymbol{\Psi}$ through the Rodrigus formula:

$$\boldsymbol{\Lambda} = \boldsymbol{I} + \frac{\sin\psi}{\psi}\tilde{\boldsymbol{\Psi}} + \frac{1-\cos\psi}{\psi^2}\tilde{\boldsymbol{\Psi}}^2 = \exp(\tilde{\boldsymbol{\Psi}}), \tag{2}$$

where $\psi = \|\boldsymbol{\Psi}\|$ is the length of the total rotation vector of the cross section. $\tilde{\boldsymbol{\Psi}} \doteq \boldsymbol{\Psi}\times$, is the anti-symmetric tensor of $\boldsymbol{\Psi}$. The position vector of a material point $\boldsymbol{X}$ in the deformed placement can be expressed as:

$$\boldsymbol{x}(t,s) = \boldsymbol{x}_c(t,s) + X_2\boldsymbol{t}_2(t,s) + X_3\boldsymbol{t}_3(t,s) = \boldsymbol{x}_c(t,s) + \boldsymbol{\Lambda}\boldsymbol{E}, \tag{3}$$

where $\boldsymbol{E} = X_2\boldsymbol{E}_2 + X_3\boldsymbol{E}_3$; $\boldsymbol{x}_c(t,s)$ is the cable center line at time t and initial arc length s, and its virtual spatial displacement is

$$\delta\boldsymbol{x} = \delta\boldsymbol{x}_c + \boldsymbol{\Lambda}\delta\tilde{\boldsymbol{\Theta}}\cdot\boldsymbol{E}, \tag{4}$$

where $\tilde{\boldsymbol{\Theta}}$ is the increment of the total rotation vector $\boldsymbol{\Psi}$. From Eq. (3), we can obtain

$$\ddot{\boldsymbol{x}} = \ddot{\boldsymbol{x}}_c + \boldsymbol{\Lambda}\tilde{\boldsymbol{\Omega}}\tilde{\boldsymbol{\Omega}}\boldsymbol{E} + \boldsymbol{\Lambda}\tilde{\boldsymbol{A}}\boldsymbol{E}, \tag{5}$$

where $\tilde{\boldsymbol{\Omega}} = \boldsymbol{\Lambda}^T\dot{\boldsymbol{\Lambda}}$ and $\tilde{\boldsymbol{A}} = \dot{\tilde{\boldsymbol{\Omega}}}$; $\boldsymbol{\Omega}$ is the material angular velocity, and $\boldsymbol{A}$ is the material angular acceleration.

2.2 Motion Equation in Weak Form

In this section, we extend the total Lagrangian formulation of geometrically exact beam theory (Cardona and Geradin, 1988; Mäkinen, 2007) to apply to the flexible umbilical cable in deep-sea ROV systems. We can classify the forces acting on the umbilical cable system into three types: (i) the internal stresses; (ii) the external forces, such as the gravity, buoyancy, and viscous drag force; (iii) the acceleration forces, like the inertia force and added mass force due to the reaction of the surrounding water particles. We can apply the principle of virtual work due to those forces to obtain the weak forms of the governing equations for the flexible umbilical cable as follows:

$$G(\boldsymbol{q},\dot{\boldsymbol{q}},\ddot{\boldsymbol{q}};\delta\boldsymbol{q})\cdot G_{\mathrm{ext}}(\boldsymbol{q};\delta\boldsymbol{q}) - G_{\mathrm{int}}(\boldsymbol{q};\delta\boldsymbol{q}) - G_{\mathrm{acc}}(\boldsymbol{q},\dot{\boldsymbol{q}},\ddot{\boldsymbol{q}};\delta\boldsymbol{q}) = 0, \tag{6}$$

where $\boldsymbol{q} = (\boldsymbol{d},\boldsymbol{\Psi})^{\mathrm{T}}$ is the general displacement, G_{int} is the internal virtual work, G_{ext} is the external virtual work, and G_{acc} is the virtual work of acceleration forces. For the ocean cable, the total

Lagrangian formulation of external virtual work can be described as:

$$G_{\text{ext}} = \int_L \delta \boldsymbol{q} \cdot \boldsymbol{F}^{\text{ext}} \mathrm{d}s, \quad \boldsymbol{F}^{\text{ext}} = \left[\bar{\boldsymbol{n}} \quad \boldsymbol{T}^{\mathrm{T}} \bar{\boldsymbol{M}} \right]^{\mathrm{T}}, \tag{7}$$

where, $\boldsymbol{T}$ is the linear transformation operator between material frame and floating frame, the external force couple $\bar{\boldsymbol{M}}$ usually can vanish due to the centerline condition as $\int_A \tilde{\boldsymbol{E}} \mathrm{d}A = 0$ (Simo, 1985; Cardona and Geradin, 1988), and the external force $\bar{\boldsymbol{n}}$ is described in Section 2.3. The total Lagrangian formulation of internal virtual work can be expressed as:

$$G_{\text{int}} = \int_L \delta \boldsymbol{\varepsilon} \cdot \boldsymbol{F}^{\text{int}} \mathrm{d}s; \ \boldsymbol{\varepsilon} = \left[\boldsymbol{\Gamma} \quad \boldsymbol{K} \right]^{\mathrm{T}}; \ \boldsymbol{F}^{\text{int}} = \left[\boldsymbol{N} \quad \boldsymbol{M} \right]^{\mathrm{T}}, \tag{8}$$

where $\boldsymbol{N}$ and $\boldsymbol{M}$ are the internal forces and couples, respectively; $\boldsymbol{\Gamma}$ and $\boldsymbol{K}$ are the linear and curvature strains, respectively; and their virtual forms can be written in terms of the virtual displacements $\delta \boldsymbol{x}_{\text{c}}$ and rotations $\delta \boldsymbol{\Psi}$ according to

$$\delta \boldsymbol{\varepsilon} = \boldsymbol{B} \cdot \delta \hat{\boldsymbol{q}}; \quad \delta \hat{\boldsymbol{q}} = \left[\delta \boldsymbol{x}_{\text{c}}' \quad \delta \boldsymbol{\Psi}' \quad \delta \boldsymbol{\Psi} \right]^{\mathrm{T}}, \tag{9}$$

where $\boldsymbol{B}$ is the geometrical relation matrix. It is assumed that the material of the umbilical cable is continuous and isotropic, and the constitution relation is linearly elastic:

$$\boldsymbol{N} = \boldsymbol{C}_n \boldsymbol{\Gamma}; \quad \boldsymbol{M} = \boldsymbol{C}_m \boldsymbol{K}, \tag{10}$$

with the axial and bending elasticity tensor using the matrix formulation are

$$\boldsymbol{C}_n = diag\left\{ EA, GA_2, GA_3 \right\}; \ \boldsymbol{C}_m = diag\left\{ GJ, EI_2, EI_3 \right\},$$

where EA is the axial stiffness; GA_2 and GA_3 are the shear stiffness along the principal axis of the cross section; GJ is the torsional rigidity; EI_2 and EI_3 are the principle bending stiffness of the cross section. The cross section area A_2 and A_3 include the shear correction coefficient, and torsional inertial tensor should be the Saint−Venant torsional stiffness, which is equal to the polar inertia moment for the circular cross section assumption here. The total Lagrangian formulation of virtual work due to the acceleration forces can be written as:

$$G_{\text{acc}} = \int_L \delta \boldsymbol{q} \cdot \boldsymbol{F}^{\text{acc}} \mathrm{d}s, \tag{11}$$

we can further decompose the acceleration force $\boldsymbol{F}^{\text{acc}}$ into two components as follows:

$$\boldsymbol{F}^{\text{acc}} = \boldsymbol{F}^{\text{acc,a}} + \boldsymbol{F}^{\text{acc,b}} = \begin{bmatrix} A\bar{\rho} \ddot{\boldsymbol{x}}_{\text{c}} \\ \boldsymbol{T}^{\mathrm{T}} \boldsymbol{J} \boldsymbol{T} \ddot{\boldsymbol{\Psi}} \end{bmatrix} + \begin{bmatrix} 0 \\ \boldsymbol{T}^{\mathrm{T}} \left(\tilde{\boldsymbol{\Omega}} \boldsymbol{J} \boldsymbol{\Omega} + \boldsymbol{J} \dot{\boldsymbol{T}} \dot{\boldsymbol{\Psi}} \right) \end{bmatrix}, \tag{12}$$

where $\bar{\rho} = \rho_{\text{c}} + C_{\text{m}} \rho_{\text{w}}$ is the effective density (including the added mass), ρ_{c} is the cable density, C_{m} is the added mass coefficient, ρ_{w} is the density of sea water, and $\boldsymbol{J}$ is the inertia tensor of cross section. By substituting Eqs. (7), (8) and (11) into Eq. (6), we can obtain the total Lagrangian formulation of the weak form of the governing equation as:

$$G = \int_L \left[\delta \boldsymbol{q} \cdot \left(\boldsymbol{F}^{\text{ext}} - \boldsymbol{F}^{\text{acc,a}} - \boldsymbol{F}^{\text{acc,b}} \right) - \delta \boldsymbol{\varepsilon} \cdot \boldsymbol{F}^{\text{int}} \right] \mathrm{d}s. \tag{13}$$

2.3 External Loading

In addition to the gravity and buoyancy, the external forces that act upon the umbilical cable also

include the velocity-related viscous drag force. And the wet weight vector per volume is given by

$$\boldsymbol{W}_{\mathrm{g}} = \left(\rho_{\mathrm{c}} - \rho_{\mathrm{w}}\right) g_0 \boldsymbol{e}_1, \tag{14}$$

where ρ_{c} is the current cable density, ρ_{w} is the density of sea water, and g_0 is the gravitational acceleration. Although the volume of cable may change, the variation of density is still small and negligible, thus the cable density is assumed to be constant. According to the relationship of transformation between two different frames of the same vector, if the velocity of a point in the center line is $\dot{\boldsymbol{x}}_{\mathrm{c}}(s,t)$ with its components in the frame $\{\boldsymbol{e}_i\}$, then the same velocity is $\boldsymbol{\Lambda}^{\mathrm{T}}\dot{\boldsymbol{x}}_{\mathrm{c}}$ with its components in the floating frame $\{\boldsymbol{t}_i\}$. In order to obtain the viscous drag force, the relative velocity between the cable and ocean current at a point should be known firstly. Here we assume that the velocity of ocean current varies with water depth *h,* which can be described in the spatial frame as:

$$\boldsymbol{V} = v_2(h)\boldsymbol{e}_2 + v_3(h)\boldsymbol{e}_3. \tag{15}$$

Then the same velocity vector $\boldsymbol{V}$ with its components in the local frame $\{\boldsymbol{t}_i\}$ can be given by

$$\hat{\boldsymbol{V}} = \boldsymbol{\Lambda}^{\mathrm{T}}\begin{bmatrix}0 & v_2 & v_3\end{bmatrix}^{\mathrm{T}} = \begin{bmatrix}\hat{V}_1 & \hat{V}_2 & \hat{V}_3\end{bmatrix}^{\mathrm{T}}, \tag{16}$$

where the subscripts correspond to the local basis t_1, t_2, and t_3. The relative velocity vector between the cable and ocean current with its components in the local frame can then be given by

$$\hat{\boldsymbol{V}}_r = \boldsymbol{\Lambda}^{\mathrm{T}}\dot{\boldsymbol{x}}_{\mathrm{c}} - \hat{\boldsymbol{V}} = \begin{bmatrix}\hat{V}_{r1} & \hat{V}_{r2} & \hat{V}_{r3}\end{bmatrix}^{\mathrm{T}}. \tag{17}$$

According to the experienced Morison formula for underwater slender body, we can obtain the viscous drag force vector $\boldsymbol{f}_{\mathrm{d}}$ with its components in the local frame $\{\boldsymbol{t}_i\}$,

$$\boldsymbol{f}_{\mathrm{d}} = \left[-\frac{1}{2}\rho_{\mathrm{w}} C_{\mathrm{D1}} \pi d \hat{V}_{r1}\left|\hat{V}_{r1}\right| \quad -\frac{1}{2}\rho_{\mathrm{w}} C_{\mathrm{D2}} d \hat{V}_{r2}\sqrt{\hat{V}_{r2}^2 + \hat{V}_{r3}^2} \quad -\frac{1}{2}\rho_{\mathrm{w}} C_{\mathrm{D3}} d \hat{V}_{r3}\sqrt{\hat{V}_{r2}^2 + \hat{V}_{r3}^2}\right]^{\mathrm{T}}, \tag{18}$$

where *d* is the cable diameter, C_{D1} is the tangent drag coefficient, and C_{D2} and C_{D3} are the normal and binormal drag coefficients, respectively. After the coordinate transformation, we can obtain the viscous drag force $\boldsymbol{F}_{\mathrm{D}}$ with its components in the spatial frame:

$$\boldsymbol{F}_{\mathrm{D}} = \boldsymbol{\Lambda} \cdot \boldsymbol{f}_{\mathrm{d}}. \tag{19}$$

From above, the total external forces that act on per unit length umbilical cable including gravity, buoyancy and viscous drag, can be summarized as:

$$\overline{\boldsymbol{n}} = \boldsymbol{W}_{\mathrm{g}} A + \boldsymbol{F}_{\mathrm{D}}. \tag{20}$$

3. Finite Element Discretization

3.1 Consistent Linearization

The weak forms of governing equations are highly nonlinear equations without direct analytical solution, and usually can be solved by the iteration/correction method like the Newton–Raphson algorithm to approach to the real solution step by step. Therefore, it is necessary to linearize those weak forms. By employing the directional derivative, we can obtain the linear part of total virtual work

(Mäkinen and Marjamäki, 2006; Mäkinen, 2007) at a given state $\boldsymbol{q}_0$ and $\dot{\boldsymbol{q}}_0$ as follows:

$$lin(G) = G_0 + \boldsymbol{D}_{\boldsymbol{q}} G_0 \cdot \Delta\boldsymbol{q} + \boldsymbol{D}_{\dot{\boldsymbol{q}}} G_0 \cdot \Delta\dot{\boldsymbol{q}}, \tag{21}$$

where, "$(\,)_0$" represents the value at the given state (the same as follows). The first term G_0 represents the residual virtual work, the second and the third terms represent the increment of virtual work. From Eqs. (21) and Eq. (7), we can obtain the linear part of the external virtual work as:

$$lin\left[G_{\text{ext}}\left(\boldsymbol{q};\delta\boldsymbol{q}\right)\right] = G_{\text{ext},0} + \boldsymbol{D}_{\boldsymbol{q}} G_{\text{ext},0} \cdot \Delta\boldsymbol{q} = \int_L \delta\boldsymbol{q} \cdot \boldsymbol{F}^{\text{ext}} \mathrm{d}s + \delta\boldsymbol{q} \cdot \boldsymbol{K}_{\text{ext}} \cdot \Delta\boldsymbol{q}, \tag{22}$$

where $\boldsymbol{K}_{\text{ext}} = \boldsymbol{D}_{\boldsymbol{q}} \boldsymbol{F}^{\text{ext}}$ is the tangential loading stiffness, characterizing the variation of tangent stiffness tensor due to the external load during the motion of large displacement. The external forces can be divided into conservative forces like weight and buoyancy and non-conservative forces like viscous drag forces. Therefore, $\boldsymbol{K}_{\text{ext}}$ can also be divided into two parts: conservative part and non-conservative part. The conservative part will vanish due to the centerline condition, while the non-conservative part is ignored in this paper since it is much smaller than other tangent stiffness tensors due to the internal forces. The linearization of the internal virtual work at the given state is given as:

$$lin(G_{\text{int}}) = G_{\text{int},0} + \boldsymbol{D}_{\dot{\boldsymbol{q}}} \bar{G}_{\text{int},0} \cdot \Delta\hat{\boldsymbol{q}} = G_{\text{int},0} + \delta\hat{\boldsymbol{q}} \cdot \int_L \left(\boldsymbol{K}_{\text{mat}} + \boldsymbol{K}_{\text{geo}}\right) \mathrm{d}s \cdot \Delta\hat{\boldsymbol{q}}, \tag{23}$$

where, $\boldsymbol{K}_{\text{mat}} = \boldsymbol{B}^{\text{T}} \boldsymbol{C}_{nm} \boldsymbol{B}$ is the material stiffness tensor, $\boldsymbol{C}_{nm} = diag\left\{\boldsymbol{C}_n, \boldsymbol{C}_m\right\}$, and $\boldsymbol{K}_{\text{geo}} = \left(\boldsymbol{D}_{\dot{\boldsymbol{q}}} \boldsymbol{B}^{\text{T}}\right) \boldsymbol{F}^{\text{int}}$ is the geometrical stiffness tensor. Both of them are symmetrical tensors, which is the important merit for numeric calculation. Finally, the linearization of the virtual work term due to acceleration forces also can be expressed at the given state as:

$$\begin{aligned} lin(G_{\text{acc}}) &= G_{\text{acc},0} + \boldsymbol{D}_{\boldsymbol{q}} G_{\text{acc},0} \cdot \Delta q + \boldsymbol{D}_{\dot{\boldsymbol{q}}} G_{\text{acc},0} \cdot \Delta\dot{\boldsymbol{q}} \\ &= \delta\boldsymbol{q} \cdot \int_L \boldsymbol{F}^{\text{acc,b}} \mathrm{d}s + \delta\boldsymbol{q} \cdot \int_L \boldsymbol{M} \mathrm{d}s \cdot \ddot{\boldsymbol{q}} + \delta\boldsymbol{q} \cdot \int_L \boldsymbol{K}_{\text{cent}} \mathrm{d}s \cdot \Delta\boldsymbol{q} + \delta\boldsymbol{q} \cdot \int_L \boldsymbol{C}_{\text{gyro}} \mathrm{d}s \cdot \Delta\dot{\boldsymbol{q}}, \end{aligned} \tag{24}$$

where $\boldsymbol{M}$ is the mass tensor. $\boldsymbol{K}_{\text{cent}}$ and $\boldsymbol{C}_{\text{gyro}}$ are the centrifugal tensor and the gyroscopic tensor, respectively, which are not significant in the ocean cable cases, and thus can be neglected unless in high speed rotation scenarios.

3.2 Finite Element Equation

In this section we discuss the discrete approximation of the foregoing linearization of the weak form based on the finite element method employing the standard isoparametric interpolations. The discrete approximation is constructed by using $n_{\text{e}} = 2$ nodes of geometrically exact beam element. The displacement and position vectors of cable center line and the total rotation vectors of cross section in the current configuration can be discretized as:

$$\begin{aligned} &\boldsymbol{\Psi} \approx \boldsymbol{\Psi}^h = \sum_{I=1}^{n_{\text{e}}} N_I\left(\xi\right) \boldsymbol{\Psi}_I; \quad \boldsymbol{d} \approx \boldsymbol{d}^h = \sum_{I=1}^{n_{\text{e}}} N_I\left(\xi\right) \boldsymbol{d}_I; \\ &\boldsymbol{x}_{\text{c}} \approx \boldsymbol{x}_{\text{c}}^h = \sum_{I=1}^{n_{\text{e}}} N_I\left(\xi\right) \boldsymbol{x}_{\text{c}I}; \quad \boldsymbol{x}_{\text{c}}' \approx \boldsymbol{x}_{\text{c}}'^h = \sum_{I=1}^{n_{\text{e}}} N_I'\left(\xi\right) \boldsymbol{x}_{\text{c}I}, \end{aligned} \tag{25}$$

where $\boldsymbol{\Psi}_I$ and $\boldsymbol{d}_I$ are the nodal value of the total rotation vector and displacement of the cable center line, respectively; $\boldsymbol{x}_{\text{c}I}$ and $\boldsymbol{x}_{\text{c}I}'$ are the nodal values of the position vector and tangential line of

the cable centerline, respectively; N_I is the nodal shape function, $N_I' = \partial N_I / \partial s$, which can be described in the parent element as:

$$N_I(\xi) = \prod_{J=1, J\neq I}^{n_e} \frac{\xi - \xi_J}{\xi_I - \xi_J}, \tag{26}$$

where ξ_I, $I \in [1, n_e]$ are the nodal values of natural coordinates. The partial derivative of the shape function to the arc length s is

$$N_I' = \frac{\partial N_I}{\partial s} = \boldsymbol{J}_a^{-1} \frac{\partial N_I}{\partial \xi}, \tag{27}$$

where $\boldsymbol{J}_a$ is the Jacobian matrix, according to the theory of arc length, we arrive at

$$\boldsymbol{J}_a(\xi) = \frac{\mathrm{d}s}{\mathrm{d}\xi} = \left\| \frac{\partial \boldsymbol{x}_c'(\xi)}{\partial \xi} \right\| = \frac{1}{2} \left\| \boldsymbol{x}_{c2} - \boldsymbol{x}_{c1} \right\|. \tag{28}$$

With these interpolations in hand, we can obtain the discrete approximation for the virtual strain measures according to

$$\delta \boldsymbol{\varepsilon} = \boldsymbol{B}_I^h \delta \boldsymbol{q}_I, \tag{29}$$

where the Einstein Summation convention is default. By substituting the finite element interpolations defined in the foregoing into the linearization of the weak form Eq. (21), we can obtain the discrete expression for an element.

$$lin(G_e^h) = G_{e,0}^h + \boldsymbol{D}_{\boldsymbol{q}} G_{e,0}^h \cdot \Delta \boldsymbol{q} + \boldsymbol{D}_{\dot{\boldsymbol{q}}} G_{e,0}^h \cdot \Delta \dot{\boldsymbol{q}}. \tag{30}$$

Firstly, we discuss the discretization of the residual term as follows:

$$\begin{aligned} G_{e,0}^h &= G_{ext,e,0}^h - G_{int,e,0}^h - G_{acc,e,0}^h \\ &= \delta \boldsymbol{q}_I \cdot \int_{L_e} \boldsymbol{N}_I^{\mathrm{T}} \boldsymbol{F}^{ext} \mathrm{d}s - \delta \boldsymbol{q}_I \cdot \int_{L_e} \boldsymbol{B}_I^{hT} \boldsymbol{F}^{int} \mathrm{d}s - \delta \boldsymbol{q}_I \cdot \int_{L_e} \boldsymbol{N}_I^{\mathrm{T}} \left(\boldsymbol{F}^{acc,b} + \boldsymbol{F}^{acc,a} \right) \mathrm{d}s \\ &= \delta \boldsymbol{q}_I \cdot \left(\boldsymbol{f}_{eI}^{ext} - \boldsymbol{f}_{eI}^{int} - \boldsymbol{f}_{eI}^{acc,b} - \boldsymbol{M}_{eIJ} \ddot{\boldsymbol{q}}_J \right), \end{aligned} \tag{31}$$

in which $\boldsymbol{N}_I = N_I \boldsymbol{I}_{6\times 6}$. $\boldsymbol{f}_{eI}^{ext}$, $\boldsymbol{f}_{eI}^{int}$ and $\boldsymbol{f}_{eI}^{acc,b}$ are nodal vectors of external, internal and acceleration force, respectively; $(\,)_{eIJ}$ denotes the element of a tensor. Similarly, the discrete approximation of the linear increment term of Eq. (30) is

$$\begin{aligned} \boldsymbol{D}_{\boldsymbol{q}} G_{e,0}^h \cdot \Delta \boldsymbol{q} + \boldsymbol{D}_{\dot{\boldsymbol{q}}} G_{e,0}^h \cdot \Delta \dot{\boldsymbol{q}} &= \delta \boldsymbol{q}_I \cdot \boldsymbol{K}_{load,eIJ} \Delta \boldsymbol{q}_J - \delta \boldsymbol{q}_I \cdot \boldsymbol{S}_{eIJ} \Delta \boldsymbol{q}_J - \delta \boldsymbol{q}_I \cdot \boldsymbol{K}_{cent,eIJ} \Delta \boldsymbol{q}_J \\ &\quad - \delta \boldsymbol{q}_I \cdot \boldsymbol{C}_{gyro,eIJ} \Delta \dot{\boldsymbol{q}}_J = \delta \boldsymbol{q}_I \cdot \boldsymbol{K}_{eIJ} \Delta \boldsymbol{q}_J - \delta \boldsymbol{q}_I \cdot \boldsymbol{C}_{gyro,eIJ} \Delta \dot{\boldsymbol{q}}_J, \end{aligned} \tag{32}$$

where the Einstein summation convention is default, and

$$\begin{aligned} &\boldsymbol{K}_{load,eIJ} = \int_{L_e} \boldsymbol{N}_I^{\mathrm{T}} \boldsymbol{K}_{load} \boldsymbol{N}_J \mathrm{d}s; \quad \boldsymbol{K}_{cent,eIJ} = \int_{L_e} \boldsymbol{N}_I^{\mathrm{T}} \boldsymbol{K}_{cent} \boldsymbol{N}_J \mathrm{d}s; \quad \boldsymbol{S}_{eIJ} = \boldsymbol{K}_{mat,eIJ} + \boldsymbol{K}_{geo,eIJ}; \\ &\boldsymbol{C}_{gyro,eIJ} = \int_{L_e} \boldsymbol{N}_I^{\mathrm{T}} \boldsymbol{C}_{gyro} \boldsymbol{N}_J \mathrm{d}s; \quad \boldsymbol{K}_{mat,eIJ} = \int_{L_e} \boldsymbol{B}_I^{h\mathrm{T}} \boldsymbol{C}_{nm} \boldsymbol{B}_J^h \mathrm{d}s; \quad \boldsymbol{K}_{geo,eIJ} = \int_{L_e} \boldsymbol{Q}_I^{\mathrm{T}} \boldsymbol{K}_{geo} \boldsymbol{Q}_J \mathrm{d}s. \end{aligned} \tag{33}$$

To avoid the locking phenomenon, the external and internal forces and their tangential tensors are computed by one-point Guass quadrature, and the acceleration force and its matrices are computed by the two-point Guass quadrature. By substituting Eqs. (31) and (32) into Eq. (30), we can obtain

$$\delta \boldsymbol{q}_I \cdot \left(\boldsymbol{R}_{eI} - \boldsymbol{M}_{eIJ} \ddot{\boldsymbol{q}}_J + \boldsymbol{K}_{eIJ} \Delta \boldsymbol{q}_J - \boldsymbol{C}_{gyro,eIJ} \Delta \dot{\boldsymbol{q}}_J \right) = 0. \tag{34}$$

Here, we define the nodal residual force of an element as:

$$\boldsymbol{R}_{eI} = \boldsymbol{f}_{eI}^{\text{ext}} - \boldsymbol{f}_{eI}^{\text{int}} - \boldsymbol{f}_{eI}^{\text{acc,b}}. \tag{35}$$

From above, we can obtain the finite element equation in an element

$$\boldsymbol{R}_{\text{e}} + \boldsymbol{K}_{\text{e}}\Delta\boldsymbol{q}_{\text{e}} - \boldsymbol{C}_{\text{e}}\Delta\dot{\boldsymbol{q}}_{\text{e}} = \boldsymbol{M}_{\text{e}}\ddot{\boldsymbol{q}}_{\text{e}}. \tag{36}$$

We can further obtain the whole finite element equation by assembling Eq. (36) just as the method used in the linear finite element procedure. For it is only discretized in the spatial domain, the whole finite element equation can also be called semi-discrete equation, it is given by

$$\boldsymbol{R}_{\text{T}} + \boldsymbol{K}_{\text{T}}\Delta\boldsymbol{q} - \boldsymbol{C}_{\text{T}}\Delta\dot{\boldsymbol{q}} = \boldsymbol{M}_{\text{T}}\ddot{\boldsymbol{q}}, \tag{37}$$

where $\boldsymbol{R}_{\text{T}}$ is the total residual force vector, $\boldsymbol{K}_{\text{T}}$ is the total stiffness tensor, $\boldsymbol{C}_{\text{T}}$ is the total damping tensor, $\boldsymbol{M}_{\text{T}}$ is the total mass tensor, $\Delta\boldsymbol{q}$ is the total displacement increment vector, $\dot{\boldsymbol{q}}$ is the total velocity increment vector, and $\ddot{\boldsymbol{q}}$ is the total acceleration vector.

3.3 Boundary Conditions

The problem discussed in the previous sections belongs to the boundary value problem in math. To solve this type of problem, necessary constraints should be specified as the boundary conditions. As the umbilical cable system is launched and recovered by the hydraulic winch aboard, the motion of the top node of umbilical is the superposition of ship motion, and winch rotation. Here we assume that the motion of the top node is the same as the ship motion and ignore the winch rotation for simplicity. We specify the displacement and velocity vectors of ship as the upper end boundary conditions.

$$\boldsymbol{q}_1^i = \boldsymbol{u}_{\text{s}}^i; \quad \dot{\boldsymbol{q}}_1^i = \boldsymbol{v}_{\text{s}}^i, \tag{38}$$

where $\boldsymbol{u}_{\text{s}}^i$ and $\boldsymbol{v}_{\text{s}}^i$ are the specified displacement and velocity vectors at time step *i* and the first node, respectively. The lower end boundary conditions are specified as a force balance equation of the cage and vehicle, which subject to the forces of gravity, buoyancy, drag and tension. We consider the cage and vehicle as a mass point that is attached to the lower end node of the umbilical cable. Its equation of motion can be simplified as:

$$\left(M_{\text{c}} + M_{\text{r}}\right)\ddot{\boldsymbol{x}}_{\text{c,end}} + C_{\text{c}}\dot{\boldsymbol{x}}_{\text{c,end}} + \boldsymbol{T}_{\text{end}} = \boldsymbol{W}_{\text{c}} + \boldsymbol{W}_{\text{r}}, \tag{39}$$

where M_{c} and M_{r} are the total effective mass (including entrained and added mass) of the cage and vehicle, respectively; C_{c} is the total drag coefficient of the cage; $\boldsymbol{T}_{\text{end}}$ is the tension in the umbilical at the cage termination; $\boldsymbol{W}_{\text{c}}$ and $\boldsymbol{W}_{\text{r}}$ are the weights minus the buoyancy of the cage and vehicle, respectively; and $\dot{\boldsymbol{x}}_{\text{c,end}}$ and $\ddot{\boldsymbol{x}}_{\text{c,end}}$ are the velocity and acceleration of the cage, respectively. When the vehicle is separated with the cage, M_{r} and $\boldsymbol{W}_{\text{r}}$ are set to be zero.

4. Generalized-α Solution

By the variable substitution: $\boldsymbol{a} = \ddot{\boldsymbol{q}}$, $\boldsymbol{v} = \dot{\boldsymbol{q}}$, $\boldsymbol{u} = \boldsymbol{q}$, the motion equation (37) then turns into

$$\boldsymbol{R}_{\text{T}} + \boldsymbol{K}_{\text{T}}\Delta\boldsymbol{u} - \boldsymbol{C}_{\text{T}}\Delta\boldsymbol{v} = \boldsymbol{M}_{\text{T}}\boldsymbol{a}, \tag{40}$$

and at time t_{n+1}, the formulation of Eq. (40) can be expressed as:

$$\boldsymbol{M}_{\mathrm{T},n}\boldsymbol{a}_{n+1}+\boldsymbol{C}_{\mathrm{T},n}\Delta\boldsymbol{v}_{n+1}-\boldsymbol{K}_{\mathrm{T},n}\Delta\boldsymbol{u}_{n+1}-\boldsymbol{R}_{\mathrm{T},n}=0. \tag{41}$$

The dynamic problems in Eq. (41) are usually solved by the direct time integration method, including the explicit method and the implicit method. The main drawback of the explicit method is that its step must not be larger than a critical step, otherwise this method will be unstable, i.e., the explicit method is conditionally stable. With the larger step size and unconditional stability, the implicit methods are usually used in engineering applications with low frequency changes, such as the Newmark-β method (Newmark, 1959), which is often used in structural mechanics and solid mechanics. However, the Newmark-β method cannot suppress high frequency noise due to the lack of numerical damping. To overcome this problem, we combine the generalized-α method proposed by Chung and Hulbert (1993) and the Newton–Raphson iterative method to solve the dynamic problems described by second-order differential equations with variable coefficient matrices. The approximation of velocity and acceleration of generalized-α method can be written as:

$$\boldsymbol{a}_{n+1}=\alpha_1\left(\boldsymbol{u}_{n+1}-\boldsymbol{u}_n\right)-\alpha_2\boldsymbol{v}_n-\alpha_3\boldsymbol{a}_n;\quad \boldsymbol{v}_{n+1}=\alpha_4\left(\boldsymbol{u}_{n+1}-\boldsymbol{u}_n\right)+\alpha_5\boldsymbol{v}_n+\alpha_6\boldsymbol{a}_n, \tag{42}$$

in which

$$\alpha_1=\frac{1}{\beta(\Delta t)^2},\ \alpha_2=\frac{1}{\beta\Delta t},\ \alpha_3=\frac{1-2\beta}{2\beta},\ \alpha_4=\frac{\gamma}{\beta\Delta t},\ \alpha_5=\left(1-\frac{\gamma}{\beta}\right),\ \alpha_6=\left(1-\frac{\gamma}{2\beta}\right)\Delta t,$$

where β and γ are parameters, and Δt is the time step. The motion equation needs some modification in this method by the weighted averaging of displacement, velocity, acceleration vectors and coefficient matrices, the iterative formulation of Eq. (41) at time t_{n+1} can be denoted by

$$\boldsymbol{M}_{\mathrm{T}}\left(\boldsymbol{u}^i_{n+\alpha}\right)\boldsymbol{a}^{i+1}_{n+\alpha}+\boldsymbol{C}_{\mathrm{T}}\left(\boldsymbol{u}^i_{n+\alpha}\right)\Delta\boldsymbol{v}^{i+1}_{n+\alpha}-\boldsymbol{K}_{\mathrm{T}}\left(\boldsymbol{u}^i_{n+\alpha}\right)\Delta\boldsymbol{u}^{i+1}_{n+\alpha}-\boldsymbol{R}_{\mathrm{T}}\left(\boldsymbol{u}^i_{n+\alpha}\right)=0, \tag{43}$$

in which

$$\begin{aligned}&\boldsymbol{u}^i_{n+\alpha}=(1-\alpha_f)\boldsymbol{u}^i_{n+1}+\alpha_f\boldsymbol{u}_n,\ \boldsymbol{a}^{i+1}_{n+\alpha}=(1-\alpha_m)\boldsymbol{a}^{i+1}_{n+1}+\alpha_m\boldsymbol{a}_n,\ \boldsymbol{v}^{i+1}_{n+\alpha}=(1-\alpha_f)\boldsymbol{v}^{i+1}_{n+1}+\alpha_f\boldsymbol{v}_n,\\&\Delta\boldsymbol{u}^{i+1}_{n+\alpha}=(1-\alpha_f)\Delta\boldsymbol{u}^{i+1}_{n+1},\ \Delta\boldsymbol{v}^{i+1}_{n+\alpha}=\alpha_4(1-\alpha_f)\Delta\boldsymbol{u}^{i+1}_{n+1},\end{aligned} \tag{44}$$

where α_f and α_m are controlling parameters, when both of them are set to zero, the generalized-α method can turn into the Newmark method. From Eq. (42), we can arrive at

$$\boldsymbol{a}^{i+1}_{n+1}=\alpha_1\left(\boldsymbol{u}^{i+1}_{n+1}-\boldsymbol{u}_n\right)-\alpha_2\boldsymbol{v}_n-\alpha_3\boldsymbol{a}_n,\quad \boldsymbol{v}^{i+1}_{n+1}=\alpha_4\left(\boldsymbol{u}^{i+1}_{n+1}-\boldsymbol{u}_n\right)+\alpha_5\boldsymbol{v}_n+\alpha_6\boldsymbol{a}_n. \tag{45}$$

By substituting Eqs. (44) and (45) into Eq. (43), we can obtain

$$\boldsymbol{K}_{\mathrm{c}}\left(\boldsymbol{u}^i_{n+\alpha}\right)\Delta\boldsymbol{u}^{i+1}_{n+1}=\boldsymbol{H}\left(\boldsymbol{u}^i_{n+\alpha},\boldsymbol{u}_n,\boldsymbol{v}_n,\boldsymbol{a}_n\right), \tag{46}$$

where

$$\begin{aligned}&\boldsymbol{K}_{\mathrm{c}}\left(\boldsymbol{u}^i_{n+\alpha}\right)=\alpha_1\left(1-\alpha_m\right)\boldsymbol{M}_{\mathrm{T}}\left(\boldsymbol{u}^i_{n+\alpha}\right)+\alpha_4\left(1-\alpha_f\right)\boldsymbol{C}_{\mathrm{T}}\left(\boldsymbol{u}^i_{n+\alpha}\right)-\left(1-\alpha_f\right)\boldsymbol{K}_{\mathrm{T}}\left(\boldsymbol{u}^i_{n+\alpha}\right);\\&\boldsymbol{H}\left(\boldsymbol{u}^i_{n+\alpha},\boldsymbol{u}_n,\boldsymbol{v}_n,\boldsymbol{a}_n\right)=\boldsymbol{R}_{\mathrm{T}}\left(\boldsymbol{u}^i_{n+\alpha}\right)-\boldsymbol{M}_{\mathrm{T}}\left(\boldsymbol{u}^i_{n+\alpha}\right)\cdot\left\{\left(1-\alpha_m\right)\left[\alpha_1\left(\boldsymbol{u}^i_{n+1}-\boldsymbol{u}_n\right)-\alpha_2\boldsymbol{v}_n-\alpha_3\boldsymbol{a}_n\right]+\alpha_m\boldsymbol{a}_n\right\}.\end{aligned}$$

From Eq. (46), we can solve that

$$\Delta \boldsymbol{u}_{n+1}^{i+1} = \left[\boldsymbol{K}_{\mathrm{c}} \left(\boldsymbol{u}_{n+\alpha}^{i} \right) \right]^{-1} \boldsymbol{H} \left(\boldsymbol{u}_{n+\alpha}^{i}, \boldsymbol{u}_{n}, \boldsymbol{v}_{n}, \boldsymbol{a}_{n} \right). \tag{47}$$

The update law of displacement, velocity and acceleration vectors can be written as:

$$\begin{cases} \boldsymbol{u}_{n+1}^{i+1} = \boldsymbol{u}_{n+1}^{i} + \Delta \boldsymbol{u}_{n+1}^{i+1}; \quad \boldsymbol{v}_{n+1}^{i+1} = \boldsymbol{v}_{n+1}^{i} + \dfrac{\gamma}{\beta h} \Delta \boldsymbol{u}_{n+1}^{i+1}; \quad \boldsymbol{a}_{n+1}^{i+1} = \boldsymbol{a}_{n+1}^{i} + \dfrac{1}{\beta h^2} \Delta \boldsymbol{u}_{n+1}^{i+1}; \\ h = \Delta t = t_{n+1} - t_{n}, \quad i = 0,\ 1,\ \cdots,\ m-1. \end{cases} \tag{48}$$

The iteration stops when the following convergence criteria are satisfied, i.e.

$$\left\| \Delta \boldsymbol{u}_{n+1}^{i} \right\| \le \varepsilon \left\| \boldsymbol{u}_{n+1}^{i+1} \right\|, \quad \varepsilon \in \left[10^{-3},\ 10^{-5} \right]. \tag{49}$$

The four parameters, $\alpha_{m,}$, α_f, β, and γ together define the generalized-α method. Based on the constraint condition presented by Chung and Hulbert (1993), these parameters can be adjusted appropriately by the trial and error method.

5. Numerical Examples

A software package termed as SIACAB has been developed to implement the presented geometrically exact formulation via the FORTRAN language. In order to demonstrate the capability of the presented formulation, the static and dynamic characteristics of an umbilical cable in a deep-sea ROV system shown in Fig. 1 are analyzed, including the static analysis of the cable system with no ship motion but steady ocean current varying with water depth, the dynamic analysis of this cable system with ship heave but without ocean current, and the dynamic analysis of the cable system with ship heave and ocean current together. In particular, we compare the performance of the two different time integration methods, i.e., the Newmark-β method and generalized-α method. For the purpose of improving the convergence rate, a simple adaptive stepping method is adopted in the final example. A uniform mesh is used for all the simulation processes. Before presenting the numerical results, a validation example is first given in the following section.

5.1 Validation Example

A deep-sea umbilical cable system is chosen as that used by Driscoll *et al.* (2000a), and its material properties are given in Table 1, which are used as the input in SIACAB. For comparison, the actual heave motion of the supporting ship and cage measured by Driscoll *et al.* (2000b) at the depth of 1730 m are used in this example. A total of 100 12-DOF elements are used to model the umbilical cable. The parameters of generalized-α method are taken as $\alpha_m = 0.125$, $\alpha_f = 0.375$, $\beta = 0.39$, and $\gamma = 0.75$, the calculation is run for 120 s, and the initial step size is taken as 0.1 s.

The comparison of heave acceleration, velocity and displacement of cage calculated by using presented formulation and measured by Driscoll *et al.* (2000b) is shown in Fig. 3a, and it can be readily seen that there is a good agreement between the calculated and measured results. As shown in Fig. 3b, the mean value of heave displacement error of the cage between the two results is –0.004 m, and its corresponding standard deviation is 0.123 m. As for the heave velocity of cage, its mean value and standard deviation are –0.002 and 0.151 m/s, respectively. And the mean value of acceleration

error of cage is −0.006 m/s^2 with its standard deviation of 0.389 m/s^2. From the three kinds of standard deviations of error sets, it can be readily found that the displacements between the calculated and measured results have the best agreement, while the accelerations between the two results have the least agreement. The measured acceleration seems smoother than the calculated since it is filtered by a low-pass filter, while the calculated acceleration is not filtered.

Table 1 Properties of the umbilical cable system

Properties	Values	Properties	Values
EA(N)	4.55×10^7	Tangent drag coefficient	0.02
GA (N)	1.9×10^7	Normal drag coefficient	2.0
EI (N·m^2)	2.5×10^3	Bi-normal drag coefficient	2.0
GJ (N·m^2)	2.1×10^3	Added mass coefficient	1.5
Cable diameter (m)	0.030	Cage weight in sea (N)	43200
Cable mass (kg/m)	3.01	Vehicle weight in sea (N)	300
Cable weight in sea (N/m)	25.4	Maximal working load (kN)	200

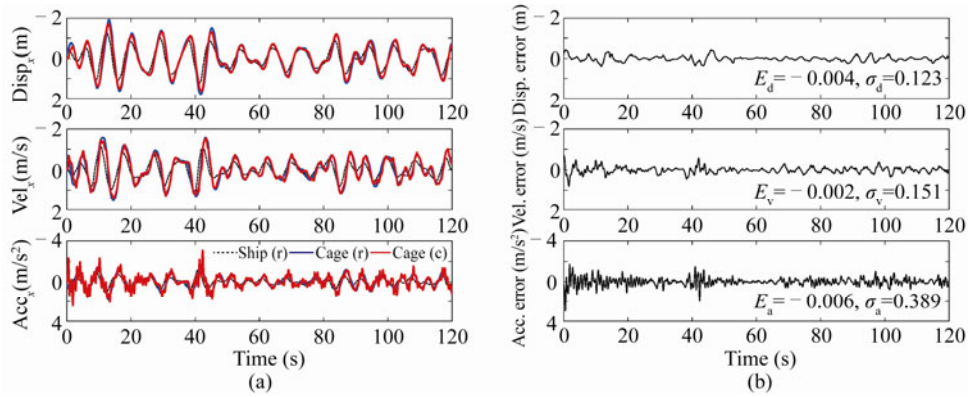

Fig. 3. (a) Comparison of cage motion between the calculated and the measured results, and (b) correspoding motion errors within 120 s. In (a), the black dash line is the measured motion of the supporting ship, the blue solid line is the measured motion of cage, and the red solid line is the calculated motion of the same cage by using the presented geometrically exact formulation.

5.2 Static Analysis in Steady Current

The different steady-state configuration of an umbilical cable in a ROV system is analyzed by using the software package SIACAB. The physical parameters of deep-sea ROV system are the same as those in Section 5.1. There are many factors affecting the umbilical cable system, such as the physical parameters of the armored umbilical cable, ocean current, and the mother ship movement. However, in this example, we only analyze the impact of ocean current on the cable system, while other factors are considered in later examples. It is assumed that ocean current depends only upon water depth, so this analysis is a quasi-static process. The ocean current profile can be expressed as:

$$\boldsymbol{V} = v_y \boldsymbol{e}_2 + v_z \boldsymbol{e}_3 = v_0 \left(1 - \frac{x}{h}\right) \boldsymbol{e}_2 + v_0 \left(1 - \frac{x}{h}\right) \boldsymbol{e}_3, \quad 0 < x < h, \tag{50}$$

where v_0 (m/s) is the current rate component of the sea surface along y and z axis, and here its value is set as 0.2, 0.5, 0.8, 1.0, and 1.2, respectively. At a given depth, there is only horizontal current parallel

to the horizontal plane, and no vertical current. The whole current linearly decreases with the increasing depth. For simplicity, we only take the component v_y into consideration, and set $v_x = 0$, $v_z = 0$ for static analysis. The case of non-zero v_z is considered in dynamic analysis. Since the maximum of diving depth of this vehicle is *h*=5000 m, we choose two typical depths of 3000 and 5000 m. The static problem is solved by Newton–Raphson method.

Fig. 4 shows the different static configurations at the depth of 3000 m in several ocean currents. It can be found that umbilical cable shifts along the current direction under the action of ocean current, and the horizontal offset increases with the increasing v_0. The steady horizontal offset of the end node of the umbilical cable is only 21.95 m when $v_0 = 0.2$ m/s, and 350.6 m when $v_0 = 0.8$ m/s, while the steady horizontal offset arrives at 787.3 m when $v_0 = 1.2$ m/s, indicating that the ocean current really has an important effect on the cable configurations. A similar situation occurs at 5000 m, as shown in Fig. 5, and it illustrates that the steady horizontal offset of the end node of umbilical cable is smaller than 17.86 m when $v_0 = 0.2$ m/s, while the horizontal offset arrives at about 658.2 m when $v_0 = 1.2$ m/s. Moreover, it can be found that the steady horizontal offset in the case of 5000 m is yet smaller than that in the case of 3000 m with the same ocean current. This is mainly because the magnitude of the weight of umbilical cable increases more than the external fluid loading upon the umbilical cable with the increasing depth.

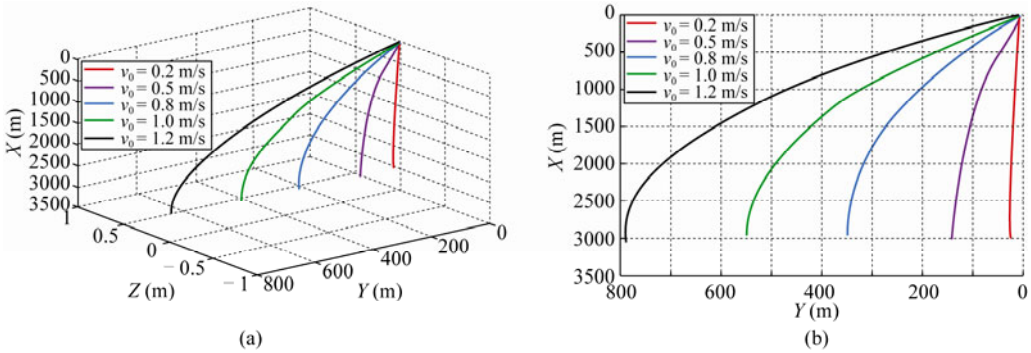

Fig. 4. Steady configurations in different depth-dependent ocean currents at the diving depth of 3000 m, (a) the three-dimensional configurations, and (b) projections in *XOY* vertical plane.

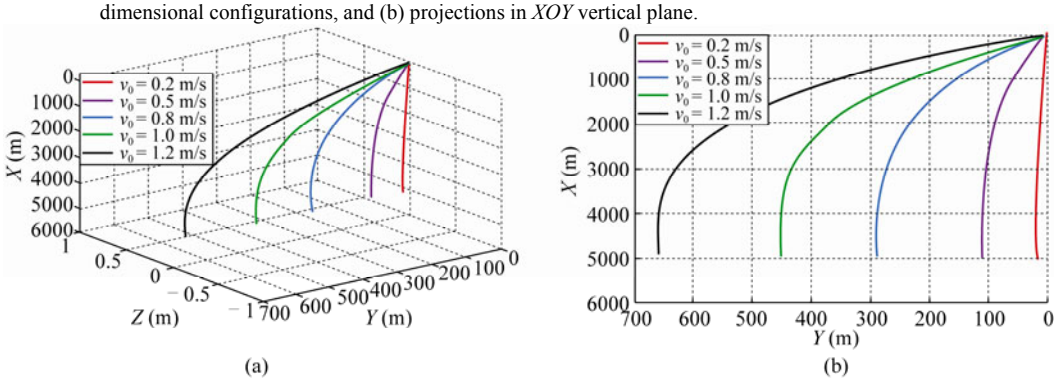

Fig. 5. Steady configurations in different depth-dependent ocean currents at the diving depth of 5000 m, (a) the three-dimensional configurations, and (b) projections in *XOY* vertical plane.

5.3 Dynamic Response with Ship Heave and Without Current

In this example, the dynamic responses of the umbilical cable system shown in Fig. 1 with only ship heave motion are analyzed, including the comparisons of displacement, velocity and acceleration between the supporting ship and cage, and the comparison of dynamic tension between both ends of umbilical cable. The physical parameters of deep-sea ROV system discussed here are the same as Section 5.1. The movement of the supporting ship under actual sea conditions is of 6 DOF motion, including the roll, pitch, yaw, heave, sway, and surge. Among them, the influence of heave motion upon the umbilical cable system is the largest, thus we only consider the heave motion of the supporting ship. The real data of ship heave motion were obtained from the "OCEAN ONE" ship at the sea state of 4 by the motion sensor OCTANS that was mounted at the pulley of A-shaped frame of the stern.

For comparison, two different algorithms, the Newmark method and the generalized-α method, are used in the simulation process. The parameters of the Newmark method take the standard values, $\alpha_m = \alpha_f = 0$, $\beta = 0.25$, and $\gamma = 0.5$. The parameters of generalized-α method is set as $\alpha_m = 0.125$, $\alpha_f = 0.375$, $\beta = 0.39$, and $\gamma = 0.75$. Each simulation is run for 100 s. The initial time step for each simulation is 0.1 s. The uniform node spacing of 10 m is used in the umbilical cable.

In this section, we also choose two typical depths of 3000 and 5000 m, and the simulated results are shown in Figs. 6–9.

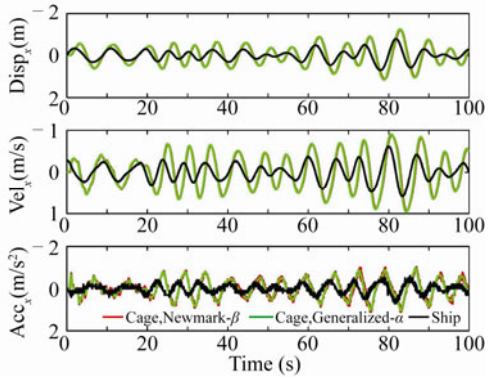

Fig. 6. Vertical displacement, velocity and acceleration of ship and cage at the diving depth of 3000 m with only ship motion.

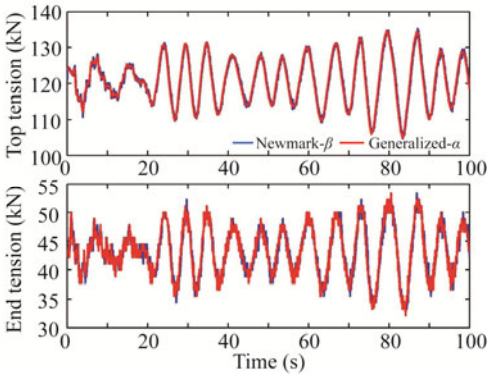

Fig. 7. Dynamic tension at both ends of the umbilical cable at the depth of 3000 m with only ship motion.

From Fig. 6, it can be found that the phase of either displacement or velocity or acceleration of the cage lags behind that of the supporting ship obviously, and the amplitudes of them are larger than that of the supporting ship. Either the displacement or the velocity of the cage for both algorithms has a good agreement, but the acceleration of the cage is obviously different for two schemes. For the Newmark-β scheme, there is too much noise in the curve of acceleration, while for the generalized-α scheme, the acceleration profile of cage becomes more stable due to the addition of numerical dissipation which can suppress the high-frequency noise considerably. From the dynamic tension profiles of both ends of umbilical cable, we can further find that the similar results are given by the two types of schemes, but the performance of generalized-α method is much better than that of the

Newmark-β scheme because of the numerical dissipation, as shown in Fig. 7, from which we can also learn that mean tension for the top node of the umbilical is 120.82 kN, and for the end node is 43.35 kN. While the static tension for the top node is 119.40 kN, and for the end node is 43.20 kN. The actual dynamic tension should fluctuate around the static tension, and must not overpass the maximum working load, or else the umbilical cable will break down.

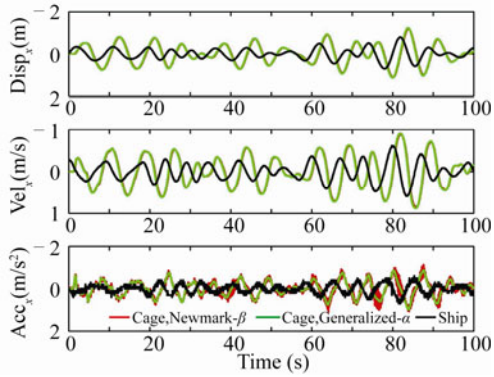

Fig. 8. Vertical displacement, velocity and acceleration of ship and cage at the diving depth of 5000 m with only ship motion.

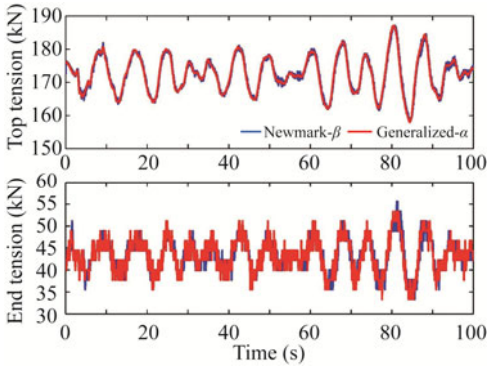

Fig. 9. Dynamic tension at both ends of umbilical cable at the depth of 5000 m with only ship motion.

From Figs. 8 and 9, through the similar rules we can find that the data profiles of generalized-α scheme are much better than those of the Newmark method in the case of the depth of 5000 m, which is the maximum depth that a deep-sea ROV can dive. Owing to its own elasticity and the increasing working depth, the stiffness of umbilical cable will decrease, and the magnitude of cage motion will be magnified with more severe phase lag during the same top excitation. Meanwhile, the mean tension at the top node increases, and the maximum tension nearly reaches the maximal working load of 200 kN, which is the critical condition that should never be passed. The mean tension at the end node changes little, because the weight of the combination of cage and underwater vehicle does not change significantly.

5.4 Dynamic Response with Ship Heave and Current

In the final example, we consider the problem of this umbilical cable system in three-dimensional horizontal current with sinusoidal ship motion at the top node of the umbilical cable. The physical parameters of the system are given in Table 1. The ship motion has a amplitude of 1.0 m and a period of 8.0 s. It is still assumed that the current profile is expressed in Eq. (50), the horizontal components v_y and v_z are nonzero, and v_0 is taken as 0.5 m/s in this example.

The difficulty with this simulation involves the joint action of ship motion and ocean current on the umbilical cable. The fixed step methods usually break down as they can easily fall into the local extreme points. To overcome this problem, a simple adaptive stepping method is used, and its basic idea is to reduce the time step when the iterations outnumber the set value n_0, or else to add the time step. Simulations are performed with two types of algorithm: the Newmark method with the parameters $\alpha_m = \alpha_f = 0$, $\beta = 0.25$, and $\gamma = 0.5$, and the generalized-α method with the parameters $\alpha_m = 0.125$,

$\alpha_f = 0.375$, $\beta = 0.39$, and $\gamma = 0.75$. The simulations are run for a maximum of 100 s with the initial time step 0.1 s. Based on these conditions, we analyze the complex dynamic characteristics of the umbilical cable system at the depth of 5000 m, including the dynamic cable configuration, tension, and motion of both ends, as shown in Figs. 10–12.

Figs. 10a and 10b illustrate the three-dimensional time-dependent dynamic configurations every other 100 time steps and their projections in *XOY* plane through the Newmark-β method and generalized-α method. It can be found that with the increasing time, the umbilical cable slowly shifts away from the initial position along the direction of the resultant velocity of three-dimensional ocean current, and the angle between the horizontal projection of those dynamic configurations and the *Y* axis is exactly 45°. We can observe that the dynamic configurations acquired by these two kinds of algorithms are not exactly the same, and in general, the total horizontal offset of the Newmark method is a little larger than that of the generalized-α method. The projection of horizontal offset of the end node in *XOY* plane reaches 9.09 m at 100 s by the Newmark method, while it is 8.85 m at 100 s by the generalized-α method.

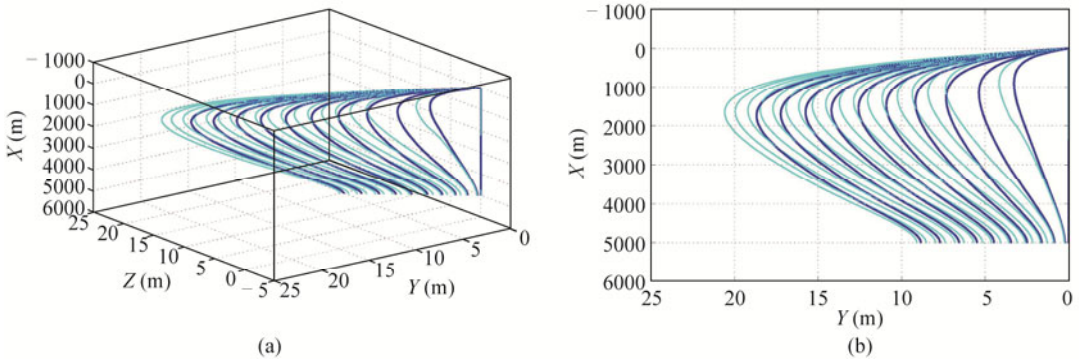

Fig. 10. (a) Three-dimensional dynamic configurations every other 100 time steps within 100 s using the generalized-α method (solid bold blue line) and Newmark-β (solid cyan line) at 5000 m, and (b) projections in *XOY* plane.

From Figs. 10a and 10b, we can also find that the cable configurations become "S" shape due to the 3D horizontal current. The reason may be that the equivalent action of the total ocean current is on the 1/3 of cable length starting from the sea surface, while the inertia of the lower part of the cable is larger than that of the upper part because of the heavy cage suspending at the end node of the cable. With the increasing time, the shape of the cable will transform from the "S" to the parabola as described in Section 5.1.

Fig. 11 illustrates that profiles obtained by the two types of algorithms are very similar. Compared with the supporting ship, the motion of the cage lags behind with obvious phase lag, and the amplitudes are all amplified. In particular, the peak displacement of the cage heave motion is continually increasing within 100 s due to the lifting action of 3D horizontal current.

Fig. 12 shows the dynamic tension of each end fluctuates around its own static tension. With respect to the Newmark-β method, the generalized-α method has the capability of numerical dissipation and the second-order accuracy, thus the data curves obtained by the generalized-α method

are more stable and with less noise. Meanwhile, it also can be seen that the maximal tension at the top node is always smaller than the maximal working load of umbilical cable, which implies that the state of umbilical cable is still in safe even under this condition.

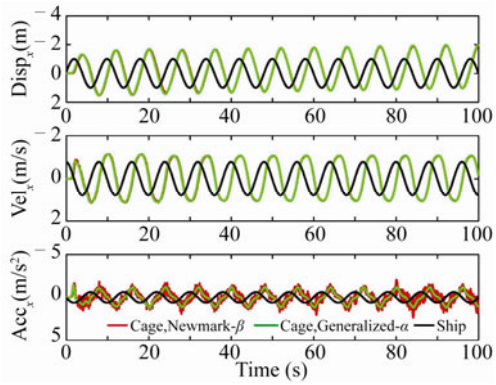

Fig. 11. Vertical displacement, velocity and acceleration of ship and cage at the depth of 5000 m with sinusoidal ship motion and depth-dependent ocean current.

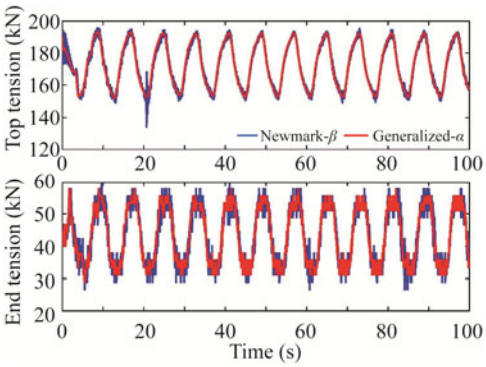

Fig. 12. Dynamic tension at both ends of the umbilical cable at the depth of 5000 m with sinusoidal ship motion and depth-dependent ocean current.

6. Conclusions

A novel three-dimensional geometrically exact formulation for underwater umbilical cable system analysis is presented, where the displacement of the cable centerline and the rotation of cross section are unknown variables. The model presented in this paper is comprehensive as it includes the effects of axial load, bend, torsion and shear, therefore, it can be applicable to the high or low tension cables. The spatial discretization is accomplished by using isoparametric interpolation of two-node finite element. The resulting governing equations expressed by the second-order differential equations with variable coefficients of matrices are solved by the generalized-α algorithm. After the validation of the presented formulation, three numerical examples are analyzed in this paper. The steady configurations of an umbilical cable system in steady ocean currents are firstly studied; then, the dynamic responses of the umbilical cable system only subjected to the ship heave motion are investigated; finally, the dynamic responses of the umbilical cable system in three-dimensional horizontal ocean current with sinusoidal ship motion are analyzed. The numerical results demonstrate the capability of the presented formulation for static and dynamic analysis of flexible umbilical cable system, and indicate that the importance of ocean current for the prediction of the umbilical cable behaviors.

References

Ablow, C. M. and Schechter, S., 1983. Numerical simulation of undersea cable dynamics, *Ocean Eng.*, **10**(6): 443–457.

Buckham, B. J., Nahon, M., Seto, M., Zhao, X. and Lambert, C., 2003a. Dynamics and control of a towed underwater vehicle system, part I: Model development, *Ocean Eng.*, **30**(4): 453–470.

Buckham, B. J., Driscoll, F. R., Nahon, M. and Radanovic, B., 2003b. Three dimensional dynamics simulation of slack tether motion in an ROV system, *Proc. 13th Int. Offshore Polar Eng. Conf.*(*ISOPE*), Honolulu, Hawaii,

USA, 127–134.

Cardona, A. and Geradin, M., 1988. A beam finite element nonlinear theory with finite rotations, *Int. J. Numer. Methods Eng.*, **26**(11): 2403–2438.

Chung, J. and Hulbert, G. M., 1993. A time integration algorithm for structural dynamics with improved numerical dissipation: The generalized-α method, *J. Appl. Mech.*, **60**(2): 371–375.

Driscoll, F. R., Lueck, R. G. and Nahon, M., 2000a. Development and validation of a lumped-mass dynamics model of a deep-sea ROV system, *Appl. Ocean Res.*, **22**(3): 169–182.

Driscoll, F. R., Lueck, R. G. and Nahon, M., 2000b. The motion of a deep-sea remotely operated vehicle system: Part 1: Motion observations, *Ocean Eng.*, **27**(1): 29–56.

Fang, Z. F., He, Q. S., Xiang, B. F., Xiao, H. P., He, K. D. and Du, Y. X., 2013. A finite element cable model and its applications based on the cubic spline curve, *China Ocean Eng.*, **27**(5): 683–692.

Feng, X. S., Li, Y. P. and Xu, H. L., 2011. The next generation of unmanned marine vehicles dedicated to the 50 anniversary of the human world record diving 10912 m, *Robot*, **33**(1): 113–118.

Gobat, J. I. and Grosenbaugh, M. A., 2006. Time-domain numerical simulation of ocean cable structures, *Ocean Eng.*, **33**(10): 1373–1400.

Mäkinen, J., 2007. Total Lagrangian Reissner's geometrically exact beam element without sigularities, *Int. J. Numer. Methods Eng.*, **70**(9): 1009–1048.

Mäkinen, J. and Marjamäki, H., 2006. Total and updated Lagrangian geometrically exact beam elements, *III European Conference on Computational Mechanics*, Springer, pp.658.

Newmark, N. M., 1959. A method of computation for structural dynamics, *J. Eng. Mech. Div.*, ASCE, **85**(3): 67–94.

Park, H. I., Jung, D. H. and Koterayama, W., 2003. A numerical and experimental study on dynamics of a towed low tension cable, *Appl. Ocean Res.*, **25**(5): 289–299.

Reissner, E., 1972. On one-dimensional finite-strain beam theory: The plane problem, *J. Appl. Math. Phys.*, **23**(5): 795–804.

Simo, J. C., 1985. A finite strain beam formulation, the three-dimensional dynamic problem, Part I, *Computer Methods in Applied Mechanics and Engineering*, **49**(1): 55–70.

Simo, J. C. and Vu-Quoc, L., 1986. A three-dimensional finite-strain rod model, Part II: Computational aspects, *Computer Methods in Applied Mechanics and Engineering*, **58**(1): 79–116.

Wu, J. and Chwang, A. T., 2001. Investigation on a two-part underwater manoeuvrable towed system, *Ocean Eng.*, **28**(8): 1079–1096.

Yan, Y., Ma, P. S., Wang, D. Y. and Gao, X. G., 2005. Development of deep sea ROV and its working system, *Robot*, **27**(1): 82–89.